scientific reports

Check for updates

OPEN

Wavelet-artificial neural network to predict the acetone sensing by indium oxide/iron oxide nanocomposites

Reza Iranmanesh[1], Afham Pourahmad[2], Danial Soltani Shabestani[3]✉, Seyed Sajjad Jazayeri[4], Hamed Sadeqi[5], Javid Akhavan[6] & Abdelouahed Tounsi[7,8]

This study applies a hybridized wavelet transform-artificial neural network (WT-ANN) model to simulate the acetone detecting ability of the Indium oxide/Iron oxide (In_2O_3/Fe_2O_3) nanocomposite sensors. The WT-ANN has been constructed to extract the sensor resistance ratio (SRR) in the air with respect to the acetone from the nanocomposite chemistry, operating temperature, and acetone concentration. The performed sensitivity analyses demonstrate that a single hidden layer WT-ANN with nine nodes is the highest accurate model for automating the acetone-detecting ability of the In_2O_3/Fe_2O_3 sensors. Furthermore, the genetic algorithm has fine-tuned the shape-related parameters of the B-spline wavelet transfer function. This model accurately predicts the SRR of the 119 nanocomposite sensors with a mean absolute error of 0.7, absolute average relative deviation of 10.12%, root mean squared error of 1.14, and correlation coefficient of 0.95813. The In_2O_3-based nanocomposite with a 15 mol percent of Fe_2O_3 is the best sensor for detecting acetone at wide temperatures and concentration ranges. This type of reliable estimator is a step toward fully automating the gas-detecting ability of In_2O_3/Fe_2O_3 nanocomposite sensors.

Atmosphere pollution by volatile organic materials[1] is a serious problem that threatens environmental protection[2] and human health[3]. Hence, it is necessary to fabricate reliable sensing devices to make the environment safe and ensure human health[4,5]. So far, different kinds of sensors such as biosensors[6], electrochemical[7], and resonant[7] have been designed for sensing purposes. The resistance-based gas detectors that utilize metal oxide semiconductors for gas sensing have been popular due to their simple operation, high sensitivity, and low cost[8–10].

The study conducted in 1962 is likely the first evidence that states absorption–desorption of gas on the metal oxide surface changes its conductivity[11]. Changing the solid measurable properties, like its resistance due to the solid–gas interaction is the essence of fabricating the electrochemical gas sensors[12]. Electrochemical sensors have a wide range of applications in the food processing industry[13], diagnosis of disease[14], medicine[15,16], monitoring toxic substances[17], and detecting explosive residuals[18] and environmental contaminants[19].

Acetone is a highly flammable organic compound irritating the skin, throat, nose, and eyes[20,21].

In recent decades, nanomaterials are used in solar cells[22], catalytic reactions[23], heat exchangers[24], wastewater treatment[25], energy application[26], and system sensing[27]. A diversity of mainly nanosized metal oxides, including tungsten oxide[28], zinc oxide[29], cobalt oxide[30], iron oxide[31], copper oxide[32], bismuth oxide[33], samarium oxide[34], and indium oxide[35] have already been used to fabricate acetone-detecting sensors. The pure and composite forms of the latest one, i.e., indium oxide (In_2O_3), have been suggested as a reliable sensor for detecting gaseous acetone[8,21,36–38].

[1]Faculty of Civil Engineering, K.N. Toosi University of Technology, No. 1346, Vali Asr Street, Mirdamad Intersection, Tehran, Iran. [2]Department of Polymer Engineering, Amirkabir University of Technology, Tehran 1591634311, Iran. [3]Department of Chemistry, Mashhad Branch, Islamic Azad University, Mashhad, Iran. [4]Department of Chemical Engineering, Abadan Azad University, Khuzestan, Iran. [5]Department of Internet and Wide Network, Iran Industrial Training Center Branch, University of Applied Science and Technology, Tehran, Iran. [6]Mechanical Engineering Department, Stevens Institute of Technology, 1 Castle Point Terrace, Hoboken, NJ 07030, USA. [7]Material and Hydrology Laboratory, Civil Engineering Department, Faculty of Technology, University of Sidi Bel Abbes, Sidi Bel Abbès, Algeria. [8]Department of Civil and Environmental Engineering, King Fahd University of Petroleum & Minerals, Dhahran 31261, Eastern Province, Saudi Arabia. ✉email: danialsoltany@yahoo.com; d.soltanishabestani@gmail.com

Experimental analyses are often expensive, time-consuming, and often contaminated with different levels of uncertainty. Therefore, it is a good idea to develop a model to estimate the acetone-detecting ability of the In_2O_3-based sensors. To the best of our knowledge, neither empirical, semi-empirical, nor intelligent methods have been suggested to automate the acetone-detecting ability of the nanocomposite sensors. Consequently, the current research applies a combination of artificial neural networks (ANN) and wavelet transform to fully automate the acetone-detecting ability of the In_2O_3/Fe_2O_3 nanocomposite sensors. The hybrid wavelet transform-artificial neural network (WT-ANN) utilizes the B-spline wavelet as a transfer function in the hidden layer of the ANN. Since the B-spline wavelet can be readily reshaped, it improves the ANN's ability to correlate a phenomenon with even a high non-linear nature. Furthermore, the WT-ANN topology has been well-tuned using the genetic algorithm and trial-and-error analysis. This scenario changes the WT-ANN structure and B-Spline shape and monitors the prediction accuracy to find the topology with the highest accuracy. Moreover, this well-tuned WT-ANN helps analyze the effect of nanocomposite chemistry, acetone concentration, and temperature on the sensor performance.

Experimental data for the acetone sensing by In_2O_3/Fe_2O_3 nanocomposites

A reliable databank should be available to construct and validate empirical[39] and semi-empirical[40] correlations and machine learning methods[41]. Hence, this study has collected 119 datasets about the acetone-detecting ability of the In_2O_3/Fe_2O_3 nanocomposite sensors from valid references[4,8,9,21]. These laboratory-scale researches have monitored the sensor resistance ratio (SRR) of the In_2O_3-based sensors in the air with respect to the acetone as a function of the nanomaterial chemistry, operating temperature, and acetone concentration[4,8,9,21]. The ranges of independent (Fe_2O_3 mole fraction in the nanocomposite sensor, operating temperature, and acetone concentration) and dependent (sensor resistance ratio) variables have been introduced in Table 1.

Figure 1 presents the histogram of independent and dependent variables gathered from the literature. This figure also reports the average and standard deviation (SD) of this collected database. Equations (1) and (2) have been utilized to calculate these statistical features[42].

$$V^{ave} = \sum_{j=1}^{N} V_j / N \tag{1}$$

$$SD = \sqrt{\sum_{j=1}^{j} \left(V_j - V^{ave}\right)^2 / N} \tag{2}$$

here, V and V^{ave} are the variable and its average value. The number of available datasets has been shown by N.

Wavelet transform-artificial neural network

Both machine and deep learning methods are trustful tools to conduct sensitivity analysis[43], parameter forecasting[44], classification[45], and control[46] purposes. As the most popular machine learning approach, an artificial neural network (ANN) can be constructed by combining several processing nodes (i.e., neurons or nodes) in some interconnected successive neuronic layers[47]. The multi-layer perceptron (MLP) is a well-established ANN type that often includes two feedforward neuronic layers, namely hidden and output[48]. Since the number of output nodes equals the number of dependent variables, it is always known[49]. On the other hand, a suitable number of hidden nodes is often found by applying the trial-and-error technique.

The artificial neuron can be viewed as a combination of linear (L) and non-linear (NL) mathematical operations. The linear part (Eq. 3) combines the multiplication of the node's entry vector (X) by the weight coefficients (W) and the bias (b).

$$L = \sum WX + b \tag{3}$$

The non-linear part is responsible for passing the linear part result through a specific equation, namely the transfer function (g). Equation (4) explains how the neuron's output (out) has been achieved.

$$Out = g(LP) \tag{4}$$

Indeed, the transfer function helps the neuron and artificial neural network to simulate non-linear problems. The main limitation of the MLP model is that it can only be equipped with some pre-defined transfer functions[50].

Independent			Dependent
Range of the Fe_2O_3 content of nanocomposite (mole fraction)	Range of temperature (K)	Range of acetone concentration (ppm)	Range of SRR (-)
0–1	453–563	8.5–1000	1.13–21

Table 1. Acetone detecting ability of the In_2O_3/Fe_2O_3 nanocomposite sensors[4,8,9,21].

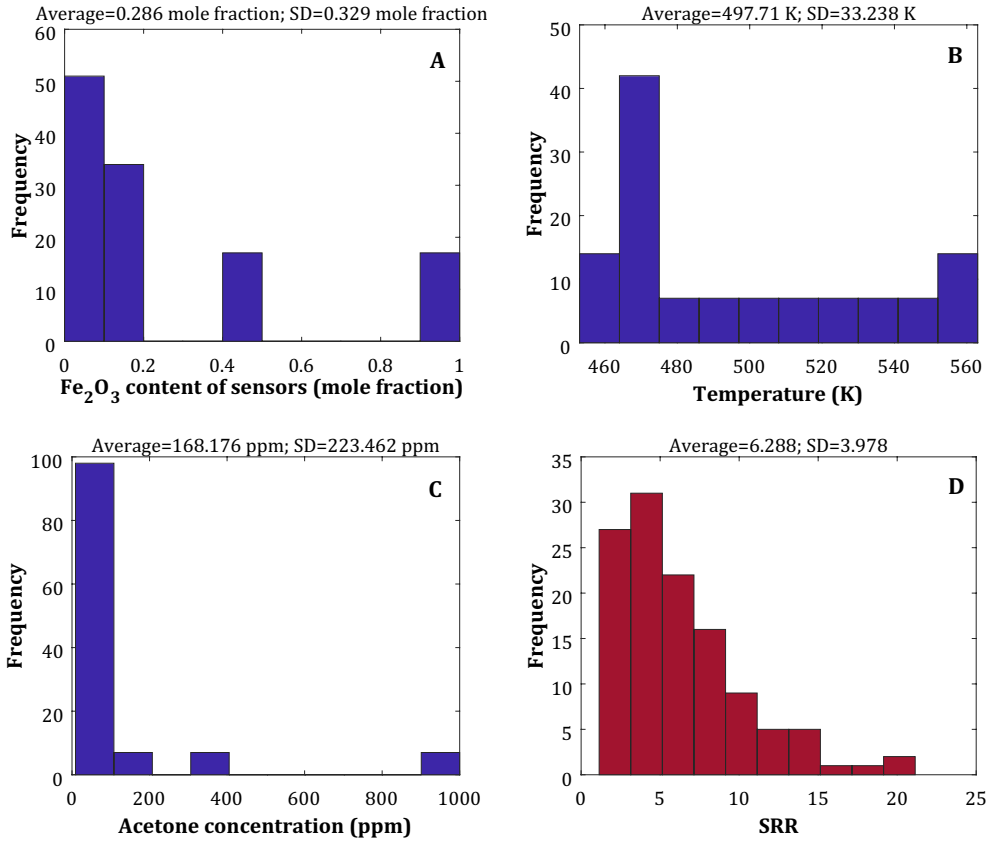

Figure 1. Histograms of the Fe_2O_3 content of nanocomposite sensors (**A**), operating temperature (**B**), acetone concentration (**C**), and SRR (**D**).

The most widely-used transfer functions, like tangent and logarithm sigmoid and radial basis, are not non-linear enough to correlate highly non-linear problems precisely.

Combining the MLP and wavelet transform

Researchers have included the wavelet transforms in the MLP body as a transfer function to build the WT-ANN model[51,52]. The B-spline wavelet is a function with tunable nonlinearity often used as a transfer function in the WT-ANN's hidden layer (g^{hid})[53]. Equations (5) and (6) show the mathematical formula of the B-spline wavelet transfer function (BSWTF)[54].

$$g^{hid}(x) = \sqrt{a}\phi(ax/\gamma)^{\gamma} \exp(2\pi i\beta x) \tag{5}$$

$$\phi(k) = \begin{cases} 1 & k = 0 \\ \sin(\pi k)/\pi k & k \neq 0 \end{cases} \tag{6}$$

where α, β, and γ are the parameters related to the nonlinearity and shape of the BSWTF. The B-spline wavelet transfer functions with different α, β, and γ values have been depicted in Fig. 2. It can be observed that this function has enough nonlinearity to correlate even the most complex phenomena. Moreover, it is possible to engineer its shape by changing its shape-related parameters[55].

Estimating acetone detecting ability of the In_2O_3/Fe_2O_3 sensor

Figure 3 presents the WT-ANN deployed to estimate the acetone-detecting ability of the In_2O_3/Fe_2O_3 sensor as a function of nanocomposite chemistry, operating temperature, and acetone concentration. It can be seen from Fig. 3 that the constructed WT-ANN constitutes an input layer and two neuronic layers of hidden and output. These layers are fully interconnected in a feedforward manner. The hidden layer has the B-spline wavelet transfer function, while the output layer equips with the linear transfer function.

This figure states that the vector of independent variables (X) is fully connected to the hidden layer's nodes by weighted links ($W^{I\to H}$). Some mathematical processes based on Eq. (7) have been imposed on the entry vector of X to the hidden layer to achieve the outlet vector (HL^{out}).

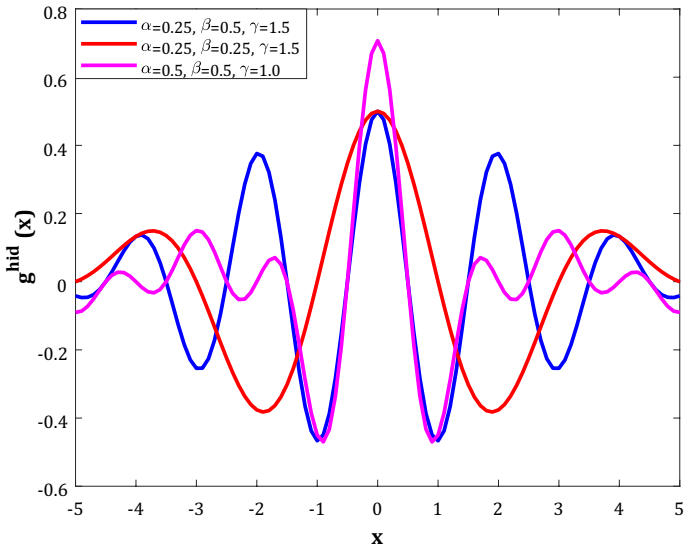

Figure 2. The general shape of the B-spline wavelet incorporated in the WT-ANN model.

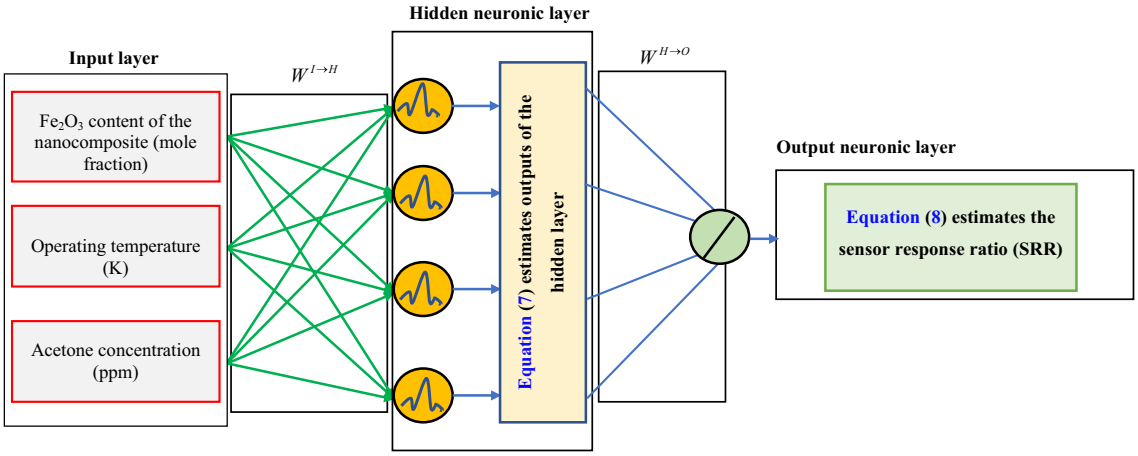

Figure 3. A typical WT-ANN with a 3-4-1 topology for estimating the acetone sensing ability of In_2O_3/Fe_2O_3 nanocomposites[56].

$$Out^{HL} = g^{hid}\left\{\left(\sum W^{I\to H} \times X - b\right)/a\right\} \tag{7}$$

The adjustable coefficients between the input and hidden layers are $W^{I\to H}$, a, and b. Equation (7) approves that the B-spline wavelet transfer function has been incorporated in the hidden layer of the WT-ANN.

Since the WT-ANN's output layer has the linear transfer function, it is possible to achieve the predicted sensor resistance ratio (SRR^{pred}) by multiplying the Out^{HL} and the weighted connections between the output and hidden layers ($W^{H\to O}$).

$$SRR^{pred} = \sum W^{H\to O} \times HL^{out} \tag{8}$$

It should be noted that the $W^{H\to O}$ shows the adjustable coefficients between the output and hidden layers.

All WT-ANN coefficients have been tuned during the cross-validation step employing an appropriate optimization algorithm[57,58]. The literature has extensively explained the tuning procedure of the $W^{I\to H}$, $W^{H\to O}$, a, and b[51].

Results and discussions

Determining the best structure of the WT-ANN

The BSWTF parameters[53] and the number of hidden nodes[51] are those structural properties of the WT-ANN that should be selected appropriately. This study uses the genetic algorithm[59] and the trial-and-error techniques to

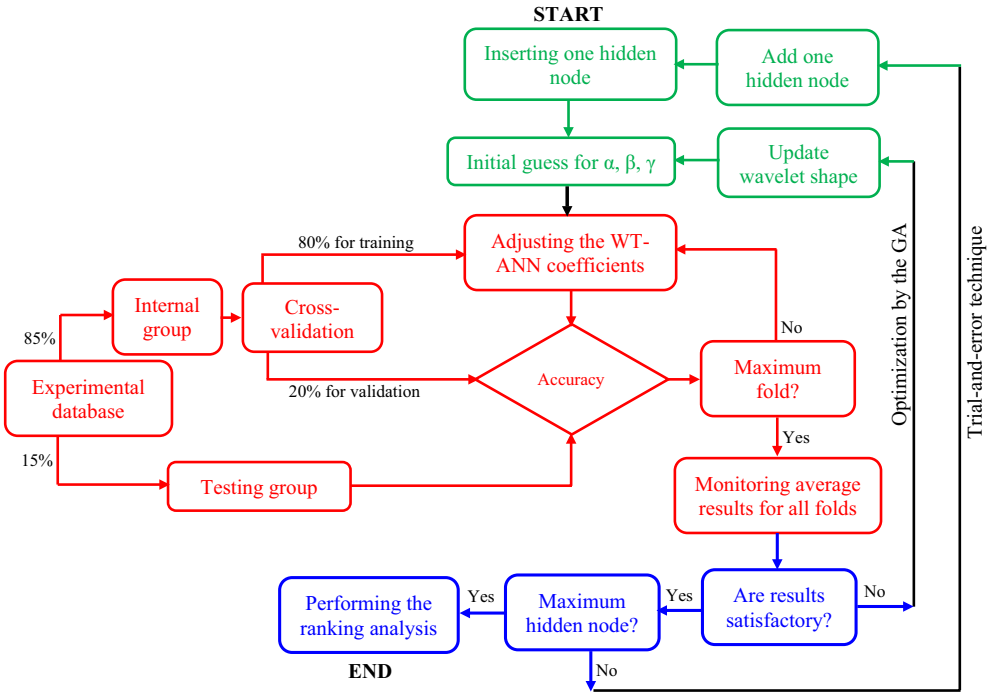

Figure 4. Constructing the WT-ANN model utilizing the trial-and-error technique and genetic algorithm (GA).

find these two structural properties, respectively. The deviation between actual and predicted SRRs is an objective function that must be minimized to construct the WT-ANN appropriately. The root mean squared error (RMSE), absolute average relative deviation (AARD%), MAE (mean absolute error), and coefficient of regression (R^2) measure this deviation. Equations (9)–(12) express the formula of MAE, R^2, MSE, and AARD%, respectively[60,61].

$$MAE = \sum_{j=1}^{N} \left| SRR^{act} - SRR^{pred} \right| / N \tag{9}$$

$$R^2 = 1 - \left(\sum_{j=1}^{N} \left(SRR^{act} - SRR^{pred} \right)_j^2 / \sum_{j=1}^{N} \left(SRR^{act} - SRR^{ave} \right)_j^2 \right) \tag{10}$$

$$RMSE = \sqrt{\sum_{j=1}^{N} \left(SRR^{act} - SRR^{pred} \right)_j^2 / N} \tag{11}$$

$$AARD\% = \sum_{j=1}^{N} \left(\left| SRR^{act} - SRR^{pred} \right| / SRR^{act} \right)_j \times 100 / N \tag{12}$$

The actual measurements, WT-ANN predictions, and average values have been shown by the superscripts of *act*, *pred*, and *ave*, respectively.

Simple flowchart of our study

Figure 4 is an understandable flowchart to explain the processes followed to design the well-tuned WT-ANN model for estimating the acetone detecting ability of the In_2O_3/Fe_2O_3 sensors. This flowchart mainly includes three separate parts as follows:

I. Constructing the WT-ANN model (green part)
II. Five-fold cross-validation (red part)
III. Comparing the WT-ANNs performance to select a model with the highest prediction accuracy (blue part)

This flowchart also has two internal and external loops for adjusting the BSWTF parameters and WT-ANN coefficients, respectively.

Number of hidden nodes	BSWTF adjusted parameters	Database	MAE	R^2	RMSE	AARD%
1	α = 0.25	Cross-validation	2.1	0.57102	3.43	28.64
	β = 0.50	Testing	1.42	0.79069	2.18	25.86
	γ = 1.50	All samples	2	0.59666	3.27	28.22
2	α = 0.35	Cross-validation	1.94	0.61594	3.29	25.8
	β = 0.35	Testing	1.93	0.80285	2.63	27.73
	γ = 1.25	All samples	1.93	0.62769	3.2	26.09
3	α = 0.30	Cross-validation	1.24	0.86345	2.07	17.2
	β = 0.20	Testing	0.97	0.92351	1.36	17.83
	γ = 1.00	All samples	1.2	0.86869	1.98	17.29
4	α = 0.15	Cross-validation	0.98	0.91765	1.63	13.83
	β = 0.40	Testing	1.23	0.80449	1.83	18.66
	γ = 1.15	All samples	1.01	0.90767	1.67	14.56
5	α = 0.50	Cross-validation	1.03	0.9073	1.7	15.26
	β = 0.45	Testing	1.49	0.79078	2.22	22.5
	γ = 1.35	All samples	1.1	0.89266	1.79	16.35
6	α = 0.10	Cross-validation	1.01	0.92789	1.53	15.02
	β = 0.75	Testing	1.16	0.86314	1.66	18.07
	γ = 1.65	All samples	1.03	0.92094	1.55	15.48
7	α = 0.75	Cross-validation	0.8	0.95192	1.33	10.99
	β = 0.65	Testing	0.8	0.91012	1.2	12.4
	γ = 1.00	All samples	0.8	0.94828	1.31	11.2
8	α = 0.25	Cross-validation	0.73	0.95681	1.12	11.72
	β = 0.50	Testing	1.31	0.85726	2.5	15.41
	γ = 1.50	All samples	0.82	0.93552	1.41	12.28
9	α = 0.50	Cross-validation	0.7	0.95889	1.17	10.1
	β = 0.50	Testing	0.69	0.95184	0.95	10.18
	γ = 1.00	All samples	0.7	0.95813	1.14	10.12
10	α = 0.30	Cross-validation	0.8	0.92995	1.42	10.7
	β = 0.20	Testing	1.07	0.96622	1.57	17.1
	γ = 1.20	All samples	0.84	0.93518	1.44	11.67

Table 2. The best results obtained by the different topologies of the wavelet neural network.

The best WT-ANN topology

It is obvious that at least one hidden node is required to build a WT-ANN with one hidden neuronic layer. Moreover, there is a rule of thumb to find the maximum allowable hidden nodes in the WT-ANN body[62]. The literature states that the numbers of the cross-validation datasets (here, 101 samples) should be at least two times the model's tunable coefficients[62]. Therefore, the WT-ANN models may be built with a maximum of ten hidden nodes. Table 2 presents the highest accurate predictions obtained by different WT-ANN topologies differing with respect to the number of hidden nodes and BSWTF shape. The accuracy of the WT-ANN models over the cross-validation and testing groups and all database has been monitored by four statistical matrices. It can be concluded that the WT-ANN with α = β = 0.5 and γ = 1.0 and nine hidden nodes (highlighted by the gray color) is the highest precise model for estimating the acetone detecting ability of the In_2O_3/Fe_2O_3 nanocomposite sensors.

Although Table 2 shows the best topology of the wavelet transform-artificial neural network, it is better to use the ranking analysis to approve this matter further. The ranking places of different WT-ANN structures in the development and validation stages have been depicted in Fig. 5. Equation (13) has been used to calculate the average rank of each WT-ANN system over the RMSE, MAE, AARD%, and R^2 indices.

$$Rank = round\left(\sum_{k=1}^{4} rank_4/4\right) \tag{13}$$

The ranking analysis also supports nine hidden nodes, and α = β = 0.5 and γ = 1.0 is the best WT-ANN topology for simulating the acetone-detecting ability of the In_2O_3/Fe_2O_3 nanocomposite sensors.

The learning algorithm's performance to tune the coefficients of the optimum WT-ANN (i.e., W, a, and b) during the five-fold cross-validation has been illustrated in Fig. 6. This figure clarifies how the mean squared error (MSE) between the actual SRRs and their counterpart predictions by the WT-ANN continuously declines by increasing the number of optimizing tries (i.e., epoch). The observed MSE eventually reaches the desired value of 0.009 after ~ 750 epochs.

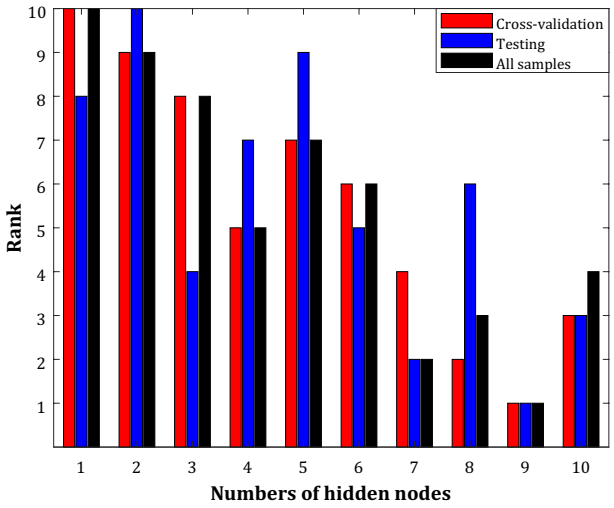

Figure 5. Rank order of different WT-ANN topologies differing from their number of hidden nodes and B-spline wavelet shape.

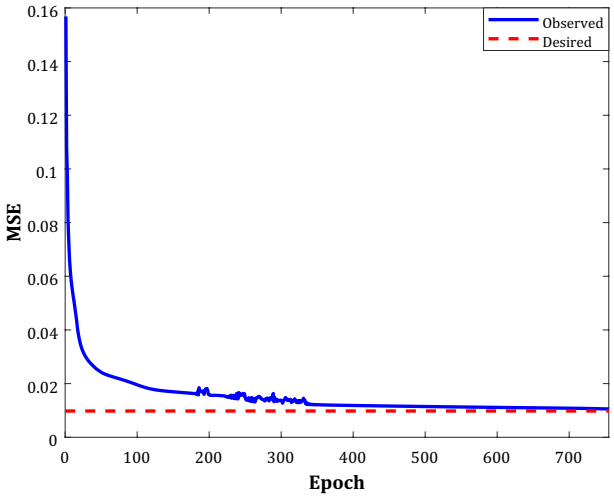

Figure 6. Decreasing the MSE by the learning algorithm in the cross-validation stage of the WT-ANN.

$$MSE = \sum_{j=1}^{N} \left(SRR^{act} - SRR^{pred}\right)_j^2 / N \tag{14}$$

Utilizing visual inspection to track the WT-ANN accuracy

Figure 7 introduces the histogram of residual error (RE) between actual and estimated SRRs in the cross-validation and testing stages. The numerical values of this residual error can be obtained from Eq. (15).

$$RE = \left(SRR^{act} - SRR^{pred}\right)_j \quad j = 1, 2, \ldots, N \tag{15}$$

This figure approves an excellent performance of the optimum WT-ANN model for monitoring the acetone sensing by the In_2O_3/Fe_2O_3 nanocomposites. The built WT-ANN successfully predicts the sensor resistance ratio by the residual error ranges from -2 to 2.5. Moreover, this analysis states that 35 cross-validation and five testing samples have been estimated with a residual error equal to zero.

The predicted SRRs by the well-structured WT-ANN model versus their laboratory-measured values in the cross-validation and testing stages have been separately indicated in Fig. 8. This figure states that the deployed WT-ANN model estimates the actual SRR values with acceptable accuracy. This finding can be highlighted as

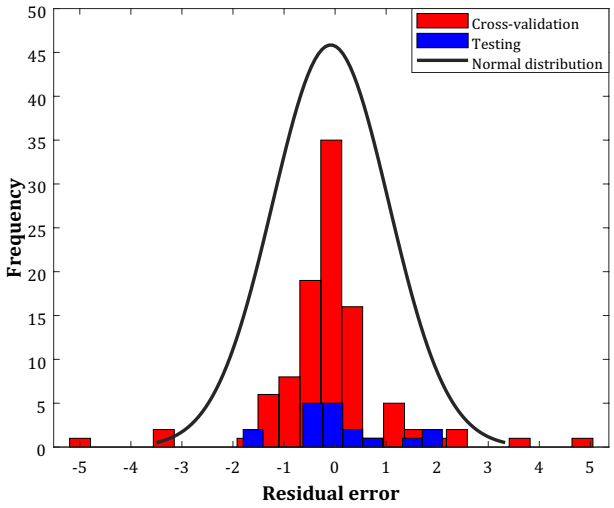

Figure 7. The histogram of the observed residual error by the optimum WT-ANN in the cross-validation and testing stages.

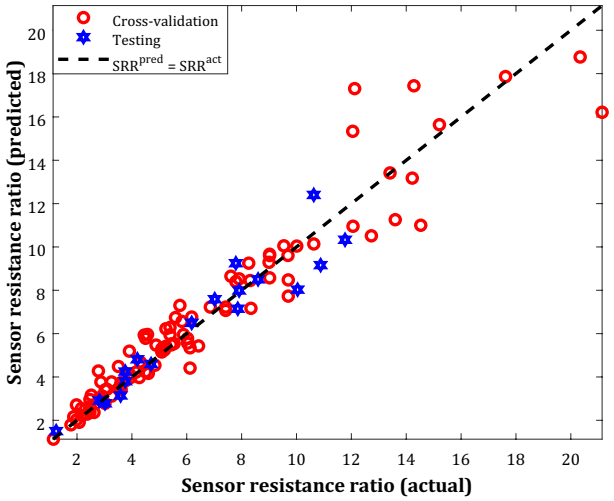

Figure 8. Correlation between predicted SRRs by the optimum WT-ANN and their related actual measurements.

a confirmation of the excellent prediction capability of the proposed WT-ANN model. Excluding five testing samples that are not estimated well, all other instances have been well-correlated.

Parametric study

The variation of the acetone detecting ability of nanocomposite sensors with different chemistry by temperature has been plotted in Fig. 9. This figure includes both experimentally reported samples and their counterpart estimations by the well-tuned WT-ANN model. A high level of agreement exists between the actual and predicted values of the sensor resistance ratios in a wide range of operating temperatures and nanocomposite chemistries.

Although pure Fe_2O_3 and In_2O_3 sensors have shown the minimum acetone detecting ability, their composites almost show better sensing performances. Generally, there is no specific trend for the acetone-detecting ability of nanocomposite with different chemistry. The acetone sensing ability of the In_2O_3-based nanocomposites increases by increasing their Fe_2O_3 molar content up to 15%, and after that, it decreases dramatically.

The In_2O_3-based nanocomposite sensor fabricated by 15 molar percent of Fe_2O_3 has the highest sensitivity for detecting the acetone agent in all temperature ranges. The $0.75In_2O_3/0.15Fe_2O_3$ nanocomposite shows its maximum SRR at 473 K (200 °C). Despite this complex behavior, the constructed WT-ANN precisely identifies the SRR variation trend and estimates relatively all individual data samples.

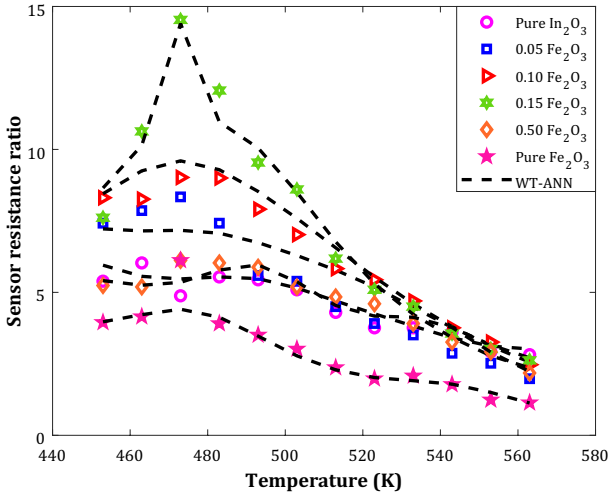

Figure 9. The influence of sensor chemistry and operating temperature on the acetone sensing (100 ppm).

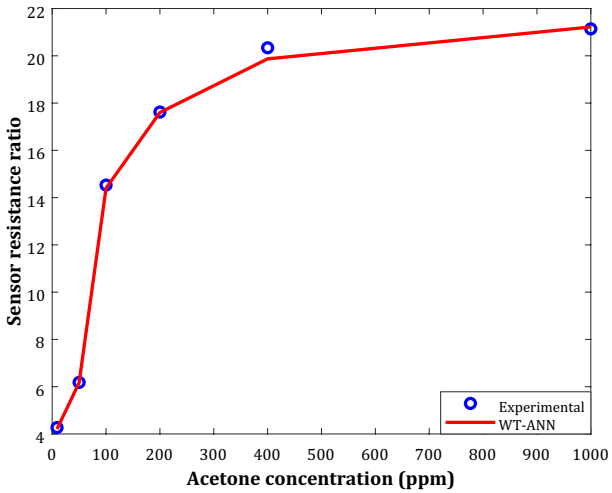

Figure 10. The effect of acetone concentration on the performance of the highest sensitive sensor (0.15 Fe_2O_3) at 473 K.

Experimental and modeling profiles of the SRR versus acetone concentration for the $0.75In_2O_3/0.15Fe_2O_3$ nanocomposite sensor have been shown in Fig. 10. This figure confirms the high compatibility between actual and estimated SRR values.

It can also be concluded that the acetone-detecting ability of the given nanocomposite continuously improves by increasing the acetone concentration. Indeed, raising the acetone concentration from 10 to 1000 ppm increases the SRR by more than 400%.

Conclusions

A straightforward intelligent correlation based on the wavelet transform-artificial neural network has been built to calculate In_2O_3/Fe_2O_3 sensor resistance ratio in the air with respect to the acetone from nanocomposite chemistry, temperature, and acetone concentration. Combining the genetic algorithm and trial-and-error analysis approved that a WT-ANN model with only nine hidden neurons and $\alpha = \beta = 0.5$ and $\gamma = 1.0$ is the highest accurate model for the considered task. The deployed WT-ANN shows an incredible performance for precisely estimating 119 SRR data points of the nanocomposites ranging from pure In_2O_3 to pure Fe_2O_3. The overall MAE = 0.7, AARD% = 10.12%, RMSE = 1.14, and $R^2 = 0.95813$ have been presented by the WT-ANN for calculating the SRR at wide ranges of acetone concentration, sensor chemistry, and temperature. The modeling results indicated that $0.75In_2O_3/0.15Fe_2O_3$ nanocomposite has the highest acetone sensing ability over wide ranges of operating conditions. The proposed WT-ANN model in this study can help full-automating the acetone detecting ability of the In_2O_3/Fe_2O_3 sensor and enhance the knowledge about the sensor behavior in different operating conditions.

Data availability

All collected data from the literature - that are analyzed in this study - are available on reasonable request from the corresponding author.

Received: 10 January 2023; Accepted: 13 February 2023
Published online: 14 March 2023

References

1. Esmaeili Faraj, S. H., Esfahany, M. N., Kadivar, M. & Zilouei, H. Vinyl chloride removal from an air stream by biotrickling filter. *J. Environ. Sci. Heal. Part A* **47**, 2263–2269 (2012).
2. Lomonaco, T. *et al.* Release of harmful volatile organic compounds (VOCs) from photo-degraded plastic debris: A neglected source of environmental pollution. *J. Hazard. Mater.* **394**, 122596 (2020).
3. Tsai, W. T. An overview of health hazards of volatile organic compounds regulated as indoor air pollutants. *Rev. Environ. Health* **34**, 81–89 (2019).
4. Liu, X. *et al.* Electrochemical sensor to environmental pollutant of acetone based on Pd-loaded on mesoporous In_2O_3 architecture. *Sens. Actuators B Chem.* **290**, 217–225 (2019).
5. Abdi, J., Esmaeili-Faraj, S. H., Mazloom, G. & Pirhoushyaran, T. Metal-organic frameworks for remediation of noxious pollutants. *Sustain. Mater. Sens. Remediat. Noxious Pollut.* 209–228 (2022).
6. Tan, J. *et al.* Screening of endocrine disrupting potential of surface waters via an affinity-based biosensor in a rural community in the Yellow River Basin, China. *Environ. Sci. Technol.* **56**, 14350–14360 (2022).
7. Sanyal, G., Vaidyanathan, A., Rout, C. S. & Chakraborty, B. Recent developments in two-dimensional layered tungsten dichalcogenides based materials for gas sensing applications. *Mater. Today Commun.* **28**, 102717 (2021).
8. Cao, E. *et al.* Acetone sensing characteristics of Fe_2O_3/In_2O_3 nanocomposite. *Mater. Lett.* **261**, 126985 (2020).
9. Wei, D. *et al.* Hydrothermal synthesis of Ce-doped hierarchical flower-like In_2O_3 microspheres and their excellent gas-sensing properties. *Sens. Actuators B Chem.* **255**, 1211–1219 (2018).
10. Wang, X., Gui, Y., Xu, L. & Chen, X. Adsorption and gas sensing properties of CuO modified $MoSe_2$ to C3F7CN decomposition products. *Mater. Today Commun.* **28**, 102677 (2021).
11. Cimino, A., Molinari, E., Cramarossa, F. & Ghersini, G. Hydrogen chemisorption and electrical conductivity of zinc oxide semiconductors. *J. Catal.* **1**, 275–292 (1962).
12. Piacente, N. P. Graphene-based gas sensor analysis for disease detection applications. M.Sc thesis, The University of Texas at Austin (2020).
13. Maduraiveeran, G., Sasidharan, M. & Ganesan, V. Electrochemical sensor and biosensor platforms based on advanced nanomaterials for biological and biomedical applications. *Biosens. Bioelectron.* **103**, 113–129 (2018).
14. Qin, J., Park, J. S., Jo, D. G., Cho, M. & Lee, Y. Curcumin-based electrochemical sensor of amyloid-B oligomer for the early detection of Alzheimer's disease. *Sens. Actuators B Chem.* **273**, 1593–1599 (2018).
15. Fan, A., Yang, G., Yang, H. & Zhao, F. Synthesis and application of dendritic Pt-Pd bimetallic nanoparticles in imprinted electrochemical sensor for the determination of florfenicol. *Mater. Today Commun.* **25**, 101448 (2020).
16. Venkatachalam, R., Annadurai, T., Nesakumar, N. & Vembu, S. Fortified electrochemical activity of $Au@Fe_3O_4$@rGO decorated GCE for sensing of acetaminophen. *Mater. Today Commun.* **27**, 102236 (2021).
17. Hryniewicz, B. M., Orth, E. S. & Vidotti, M. Enzymeless PEDOT-based electrochemical sensor for the detection of nitrophenols and organophosphates. *Sens. Actuators B Chem.* **257**, 570–578 (2018).
18. Castro, S. V. F., Cardoso, R. M., Santana, M. H. P., Richter, E. M. & Munoz, R. A. A. Graphite sheet as a novel material for the collection and electrochemical sensing of explosive residues. *Talanta* **203**, 106–111 (2019).
19. Khanmohammadi, A. *et al.* An overview to electrochemical biosensors and sensors for the detection of environmental contaminants. *J. Iran. Chem. Soc.* **17**, 2429–2447 (2020).
20. Srinivasan, P. *et al.* Development of an acetone sensor using nanostructured Co_3O_4 thin films for exhaled breath analysis. *RSC Adv.* **9**, 30226–30239 (2019).
21. Guo, L. *et al.* Ultra-sensitive sensing platform based on Pt-ZnO-In_2O_3 nanofibers for detection of acetone. *Sens. Actuators B Chem.* **272**, 185–194 (2018).
22. Sheikholeslami, M. & Ebrahimpour, Z. Thermal improvement of linear Fresnel solar system utilizing Al_2O_3-water nanofluid and multi-way twisted tape. *Int. J. Therm. Sci.* **176**, 107505 (2022).
23. Zhang, L., Li, Y., Guo, J., Kan, Z. & Jia, Y. Catalytic ozonation mechanisms of Norfloxacin using Cu–$CuFe_2O_4$. *Environ. Res.* **216**, 114521 (2023).
24. Ghazanfari, V., Imani, M., Shadman, M. M., Amini, Y. & Zahakifar, F. Numerical study on the thermal performance of the shell and tube heat exchanger using twisted tubes and Al_2O_3 nanoparticles. *Prog. Nucl. Energy* **155**, 104526 (2023).
25. Modabberasl, A., Pirhoushyaran, T. & Esmaeili-Faraj, S. H. Synthesis of $CoFe_2O_4$ magnetic nanoparticles for application in photocatalytic removal of azithromycin from wastewater. *Sci. Rep.* **12**, 19171 (2022).
26. Zhao, G., Shi, L., Yang, G., Zhuang, X. & Cheng, B. 3D fibrous aerogels from 1D polymer nanofibers for energy and environmental applications. *J. Mater. Chem. A* (2023).
27. Wang, Z., Liu, X., Ni, S.-Q., Zhuang, X. & Lee, T. Nano zero-valent iron improves anammox activity by promoting the activity of quorum sensing system. *Water Res.* **202**, 117491 (2021).
28. Liu, S., Zhang, F., Li, H., Chen, T. & Wang, Y. Acetone detection properties of single crystalline tungsten oxide plates synthesized by hydrothermal method using cetyltrimethyl ammonium bromide supermolecular template. *Sens. Actuators B Chem.* **162**, 259–268 (2012).
29. Van Duy, L., Van Duy, N., Hung, C. M., Hoa, N. D. & Dich, N. Q. Urea mediated synthesis and acetone-sensing properties of ultrathin porous ZnO nanoplates. *Mater. Today Commun.* **25**, 101445 (2020).
30. Zhang, D., Yang, Z., Wu, Z. & Dong, G. Metal-organic frameworks-derived hollow zinc oxide/cobalt oxide nanoheterostructure for highly sensitive acetone sensing. *Sens. Actuators B Chem.* **283**, 42–51 (2019).
31. Han, D. & Zhao, M. Facile and simple synthesis of novel iron oxide foam and used as acetone gas sensor with sub-ppm level. *J. Alloys Compd.* **815**, 152406 (2020).
32. Lee, J. E. *et al.* ZnO-CuO core-hollow cube nanostructures for highly sensitive acetone gas sensors at the ppb level. *ACS Appl. Mater. Interfaces* **12**, 35688–35697 (2020).
33. Shinde, P. V. *et al.* Room-temperature successive ion transfer chemical synthesis and the efficient acetone gas sensor and electrochemical energy storage applications of Bi_2O_3 nanostructures. *New J. Chem.* **42**, 12530–12538 (2018).
34. Zhang, Y. *et al.* Gas sensor based on samarium oxide loaded mulberry-shaped tin oxide for highly selective and sub ppm-level acetone detection. *J. Colloid Interface Sci.* **531**, 74–82 (2018).
35. Chen, F. *et al.* Template-free synthesis of cubic-rhombohedral-In_2O_3 flower for ppb level acetone detection. *Sens. Actuators B Chem.* **290**, 459–466 (2019).

36. Liu, W. *et al.* Rationally designed mesoporous In_2O_3 nanofibers functionalized Pt catalysts for high-performance acetone gas sensors. *Sens. Actuators B Chem.* **298**, 126871 (2019).
37. Liu, X. *et al.* Facile preparation of hierarchical Sb-doped In_2O_3 microstructures for acetone detection. *Sens. Actuators B Chem.* **270**, 304–311 (2018).
38. Kohli, N., Hastir, A., Kumari, M. & Singh, R. C. Hydrothermally synthesized heterostructures of In_2O_3/MWCNT as acetone gas sensor. *Sens. Actuators A Phys.* **314**, 112240 (2020).
39. Dasmahapatra, A. & Kroll, P. Modeling amorphous silicon nitride: A comparative study of empirical potentials. *Comput. Mater. Sci.* **148**, 165–175 (2018).
40. Wang, H. *et al.* Constitutive modelling for strain–hardening alloys during isothermal compression: An efficient semi-empirical method coupling the effects of strain, temperature and strain-rate. *Mater. Today Commun.* **24**, 101040 (2020).
41. Abdollahi, F., Hosseini, S., Sabet, M., Esmaeili-Faraj, S. H. & Amiri, F. A novel study of the gas lift process using an integrated production/injection system using artificial neural network approach. *Model. Earth Syst. Environ.* **7**, 2101–2112 (2021).
42. Fenjan, R. M., Ahmed, R. A. & Faleh, N. M. Nonlocal nonlinear dynamic behavior of composite piezo-magnetic beams using a refined higher-order beam theory. *Steel Compos. Struct.* **35**, 545–554 (2020).
43. Gajewski, J. & Sadowski, T. Sensitivity analysis of crack propagation in pavement bituminous layered structures using a hybrid system integrating Artificial Neural Networks and Finite Element Method. *Comput. Mater. Sci.* **82**, 114–117 (2014).
44. Si, Z., Yang, M., Yu, Y. & Ding, T. Photovoltaic power forecast based on satellite images considering effects of solar position. *Appl. Energy* **302**, 117514 (2021).
45. Moosavi, S. R., Vaferi, B. & Wood, D. A. Auto-detection interpretation model for horizontal oil wells using pressure transient responses. *Adv. Geo Energy Res.* **4**, 305–316 (2020).
46. Zhang, H. *et al.* Observer-based adaptive fuzzy hierarchical sliding mode control of uncertain under-actuated switched nonlinear systems with input quantization. *Int. J. Robust Nonlinear Control* **32**, 8163–8185 (2022).
47. Tang, F., Niu, B., Zong, G., Zhao, X. & Xu, N. Periodic event-triggered adaptive tracking control design for nonlinear discrete-time systems via reinforcement learning. *Neural Netw.* **154**, 43–55 (2022).
48. Lan, Q. *et al.* Artificial neural network approach for mechanical properties prediction of as-cast A380 aluminum alloy. *Mater. Today Commun.* **31**, 103301 (2022).
49. Mohammadi, M. R. *et al.* Application of robust machine learning methods to modeling hydrogen solubility in hydrocarbon fuels. *Int. J. Hydrog. Energy* **47**, 320–338 (2022).
50. Hagan, M. T., Demuth, H. B. & Beale, M. *Neural Network Design* (PWS Publishing Co., 1997).
51. Fan, Z. *et al.* Wavelet neural network modeling for the retention efficiency of sub-15 nm nanoparticles in ultrafiltration under small particle to pore diameter ratio. *J. Memb. Sci.* **635**, 119503 (2021).
52. Mohanty, D. K. & Singru, P. M. Fouling analysis of a shell and tube heat exchanger using local linear wavelet neural network. *Int. J. Heat Mass Transf.* **77**, 946–955 (2014).
53. Teolis, A. & Benedetto, J. J. *Computational Signal Processing with Wavelets* Vol. 182 (Springer, 1998).
54. Zhang, Q. & Benveniste, A. Wavelet Networks. *IEEE Trans. Neural Netw.* **3**, 889–898 (1992).
55. Hajiabotorabi, Z., Kazemi, A., Samavati, F. F. & Maalek Ghaini, F. M. Improving DWT-RNN model via B-spline wavelet multiresolution to forecast a high-frequency time series. *Expert Syst. Appl.* **138**, 112842 (2019).
56. Zhu, Y., Wang, H. & Vano, K. Applying the wavelet neural network to estimate hydrogen dissolution in underground sodium chloride solutions. *Int. J. Hydrog. Energy* **47**, 22720–22730 (2022).
57. Amini, Y. *et al.* Optimization of liquid-liquid extraction of calcium with a serpentine microfluidic device. *Int. Commun. Heat Mass Transf.* **140**, 106551 (2023).
58. Li, P., Yang, M. & Wu, Q. Confidence interval based distributionally robust real-time economic dispatch approach considering wind power accommodation risk. *IEEE Trans. Sustain. Energy* **12**, 58–69 (2020).
59. Amini, Y., Gerdroodbary, M. B., Pishvaie, M. R., Moradi, R. & Monfared, S. M. Optimal control of batch cooling crystallizers by using genetic algorithm. *Case Stud. Therm. Eng.* **8**, 300–310 (2016).
60. Zhang, H., Zou, Q., Ju, Y., Song, C. & Chen, D. Distance-based support vector machine to predict DNA N6- methyladenine modification. *Curr. Bioinform.* **17**, 473–482 (2022).
61. Shafiq, A., Çolak, A. B. & Sindhu, T. N. Analyzing activation energy and binary chemical reaction effects with artificial intelligence approach in axisymmetric flow of third grade nanofluid subject to Soret and Dufou. *Heat Transf. Res.* **54**, 75–94 (2022).
62. Jin, R., Huang, H., Li, L., Zhu, L. & Liu, Z. Energy saving strategy of the variable-speed variable-displacement pump unit based on neural network. *Procedia CIRP* **80**, 84–88 (2019).

Author contributions

R.I. collect the data and created pretty graphs. A.P., D.S.S., and S.J., developed the models. H.S. performed statistical analyses. J.A. wrote and edited manuscript. A.T. supervisionData availability. All collected data from the literature—that are analyzed in this study—are available on reasonable request from the corresponding author.

Competing interests

The authors declare no competing interests.

Additional information

Correspondence and requests for materials should be addressed to D.S.S.

Reprints and permissions information is available at www.nature.com/reprints.

Publisher's note Springer Nature remains neutral with regard to jurisdictional claims in published maps and institutional affiliations.